

The absorption factor of crystalline silicon PV cells: A numerical and experimental study

R. Santbergen*, R.J.C. van Zolingen

Department of Mechanical Engineering, Eindhoven University of Technology, P.O. Box 513, 5600MB Eindhoven, The Netherlands

Received 2 July 2007; accepted 22 October 2007

Available online 26 November 2007

Abstract

The absorption factor of a PV cell is defined as the fraction of incident solar irradiance that is absorbed by the cell. This absorption factor is one of the major parameters determining the cell temperature under operational conditions. Experimentally the absorption factor can be derived from reflection and transmission measurements. The spectral reflection and transmission factors were measured for a set of crystalline silicon (c-Si) samples with a gradually increasing complexity. The experimental results agree very well with the results from a 2D numerical model that was developed. It was found that the AM1.5 absorption factor of a typical encapsulated c-Si photovoltaic cell is as high as 90.5%. Insight was gained in the cell parameters that influence this absorption factor. The presence of texture at the front of the c-Si wafer of sufficient steepness is essential to achieve such a high absorption factor. Sub-bandgap solar irradiance ($\lambda > 1.1 \mu\text{m}$) is mainly absorbed in the very thin emitter by means of free-carrier absorption. By minimizing reflective losses over the entire solar spectrum, the AM1.5 absorption of c-Si cells can theoretically be increased to 93.0%. The effect on the annual yield of PV and PV/thermal systems is quantified.

© 2007 Elsevier B.V. All rights reserved.

Keywords: Absorption factor; Crystalline silicon solar cells; Optical model

1. Introduction

A fraction A of the solar irradiance incident on an opaque photovoltaic (PV) solar cell is absorbed and converted into electricity and heat and the remaining fraction R is reflected and lost. Gaining insight in the factors determining the absorption factor A is important for two reasons. Firstly, in PV applications the absorption factor is one of the major parameters determining the solar cell temperature under operational conditions and therefore influences the cell efficiency [1] and so the electrical yield. Secondly, the absorption factor of solar cells applied in so-called Photovoltaic/Thermal (PVT) combi-panels [2] is of major importance [3,4]. In these panels the energy not used in the PV conversion process, is collected in the form of heat, which can be used for example for domestic tap water heating and space heating [2]. Thus in a PVT

combi-panel the PV cells generate electricity and also operate as a thermal absorber. Hence the *thermal* efficiency of PVT panels and therefore the annual yield of the complete PVT system is proportional to the absorption factor to a great extent.

Because solar cells are semiconductor devices, solar cells are spectrally selective absorbers, implying that in principle the absorption factor of the absorbers in a PVT combi-panel is lower than the absorption factor of a black absorber in a conventional solar thermal collector. Because of band-to-band absorption, the absorption coefficient for photons with an energy larger than the bandgap is in general quite high. The absorption occurring for photon energies smaller than the bandgap is mainly free-carrier absorption and the free-carrier absorption coefficient is proportional to the local carrier concentration [5]. Because of the limited thickness of the regions with high free-carrier concentrations (like the emitter) this absorption mechanism is relatively weak. Hence the degree of optical confinement will have a strong influence on the

*Corresponding author. Tel.: +31 40 2472320; fax: +31 40 2475399.

E-mail address: r.santbergen@tue.nl (R. Santbergen).

Nomenclature*Latin symbols*

a	relative surface area (dimensionless)
A	AM1.5 absorption factor (dimensionless)
A_λ	spectral absorption factor (dimensionless)
c	doping concentration (1 cm^{-3})
C	areal doping concentration (1 cm^{-2})
d	layer thickness (μm)
G	solar irradiance (W m^{-2})
h	textured height (μm)
i	imaginary unit (dimensionless)
k	extinction coefficient (dimensionless)
K	cell temperature–irradiance proportionality constant ($^\circ\text{C W}^{-1}\text{ m}^2$)
N	complex refractive index (dimensionless)
n	real refractive index (dimensionless)
q	dimensionless irradiance flux (dimensionless)
\mathbf{q}	dimensionless irradiance flux vector (dimensionless)
r	reflection coefficient (dimensionless)
\mathbf{r}	matrix of reflection coefficients (dimensionless)
R	AM1.5 reflection factor (dimensionless)
R_λ	spectral reflection factor (dimensionless)
S_λ	Air Mass 1.5 solar spectrum ($\text{W m}^{-2}\mu\text{m}^{-1}$)
t	transmission coefficient (dimensionless)
\mathbf{t}	matrix of transmission coefficients (dimensionless)
T	AM1.5 transmission factor (dimensionless)
T	temperature ($^\circ\text{C}$)
T_λ	spectral transmission factor (dimensionless)
w	texture width (μm)
z	layer normal coordinate (m)

Greek symbols

α	absorption coefficient (1 cm^{-1})
β	electrical efficiency temperature coefficient ($^\circ\text{C}^{-1}$)

γ	texture steepness ($^\circ$)
δ	relative reduction in electrical efficiency (dimensionless)
η	efficiency (dimensionless)
θ_{in}	angle of incidence ($^\circ$)
θ_{r}	angle of reflection ($^\circ$)
θ_{t}	angle of transmission ($^\circ$)
λ	vacuum wavelength (μm)
τ	layer transmission coefficient (dimensionless)
$\boldsymbol{\tau}$	matrix of layer transmission coefficients (dimensionless)
ϕ	zenith angle ($^\circ$)

Sub- and superscripts

a	incident from above
ac	active cell area
ARC	anti-reflective coating
b	exiting above
back	back of the wafer
c	incident from below
cell	complete cell area
d	exiting below
eff	effective
el	electrical
fc	free-carrier absorption
front	front of the wafer
gr	cell grid area
i	angular interval number
j	angular interval number
n	n-type doping
p	p-type doping
Si	silicon
STC	standard test conditions
y	interface or layer number
Y	final interface number
+	incident irradiance from above
–	incident irradiance for below

spectral absorption factor for photons with an energy smaller than the bandgap, i.e. for long wavelength solar irradiance.

This paper deals with the absorption factor of crystalline silicon (c-Si) PV cells. Cells are considered including features to optimize light trapping and optical confinement like texturization and the applications of diffusively reflecting back surfaces. These features are present in modern cell designs. A consequence of these features is that irradiance can travel a complicated path before either being absorbed or being reflected.

Optical models for solar cells were developed by Krauter and Hanitsch [6], Fraidenraich and Vilela [7] and Lu and

Yao [8]. These models were developed for planar structures and do not take into account features like texturization and optical confinement. Optical/electrical models exist, like PC1D [9] for the electrical efficiency of c-Si solar cells, but these models focus on the wavelength region relevant for the PV conversion process, i.e. $\lambda < 1.2\mu\text{m}$. In this paper a numerical optical model for the absorption factor is presented which also focusses on the absorption processes occurring for the long-wavelength part of the solar spectrum ($\lambda > 1.2\mu\text{m}$) which contains approximately 20% of the total energy in the solar spectrum. Special attention is paid to optical confinement, the role of free-carrier absorption and back contact.

First the optical model obtained is validated by comparing the numerical results to results of optical measurements carried out on various c-Si PV cell structures. The model is then used to acquire quantitative insight in the contributions of the various absorption mechanisms to the total absorption factor. c-Si solar cells possess various design features affecting the absorption factor such as the type of front texture or the metal grid coverage. The optical model is also used to investigate the absorption factor of various solar cell designs. It will turn out that the pursuit of high electrical efficiencies in most cases will result in an increase of their absorption factor and thus in an increase of the operational cell temperature. Annual yield models exist for PV [10] and PVT systems [11–13]. Both a PV and a PVT model will be used to study effects of the increased temperature on the annual yield.

2. Model description

In the numerical model a PV cell is represented by a two-dimensional (2D) multi-layer structure as shown in Fig. 1. The laws of optics are used to determine how incident irradiance propagates through this structure. The absorbed fraction at wavelength λ , i.e. the spectral absorption factor A_λ , is determined taking into account the effects of an anti-reflective (AR) coating, scattering by rough interfaces and multiple reflections of trapped irradiance. This is done for a range of wavelengths, i.e. $\lambda = 0.3\text{--}3.0\mu\text{m}$. By averaging the spectral absorption factor A_λ over the AM1.5 spectrum S_λ [14], the (AM1.5) absorption factor A is found,

$$A = \frac{\int A_\lambda S_\lambda d\lambda}{\int S_\lambda d\lambda}. \quad (1)$$

First in Section 2.1 the optical constants that play a role are introduced. In Section 2.2 it is explained how the spectral absorption factor A_λ can be determined for a multi-layer configuration with flat and smooth interfaces. This is only a simple representation of a PV cell in which the important optical effects of rough and textured interfaces are not yet taken into account. Next in Section 2.3 it is indicated how these effects can be characterized using a matrix description. Finally in Section 2.4 it will be explained how these matrices are used in the extended model, to determine A_λ for more realistic representations of a PV cell.

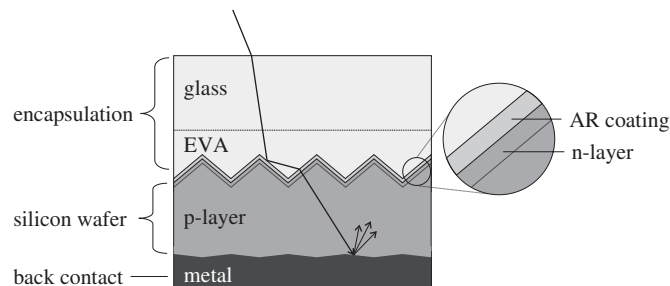


Fig. 1. A schematic cross-section of an encapsulated c-Si PV cell.

2.1. The optical constants

In the model a PV cell is represented by a multi-layer structure, each layer being characterized by a complex refractive index,

$$N = n - ik, \quad (2)$$

where both the real refractive index n and the extinction coefficient k are functions of λ . For most materials $n(\lambda)$ and $k(\lambda)$ can be found in literature [15,16]. Note that the absorption coefficient α and the extinction coefficient k are related by,

$$\alpha = 4\pi k / \lambda. \quad (3)$$

For intrinsic c-Si $\alpha(\lambda)$ is given as the solid line in Fig. 2 [17]. It can be observed that α decreases strongly with increasing wavelength. Short-wavelength photons ($\lambda < 1.0\mu\text{m}$) have an energy larger than the bandgap, hence are able to create electron–hole pairs and are readily absorbed by the crystalline silicon (c-Si). However, long-wavelength photons ($\lambda > 1.2\mu\text{m}$) cannot generate electron–hole pairs and are hardly absorbed. Photons in the transition region ($1.0\mu\text{m} < \lambda < 1.2\mu\text{m}$) are weakly absorbed, i.e. are only absorbed after having traveled some distance in the c-Si material.

By adding n- or p-type doping to a semiconductor ‘free’ electrons or holes are introduced. These free charge carriers can also absorb photons (but electron–hole pairs are not generated). Hence the absorption coefficient of silicon is a function of n- and p-type doping concentration c_n and c_p . Green [5] gives the following expression for the free-carrier

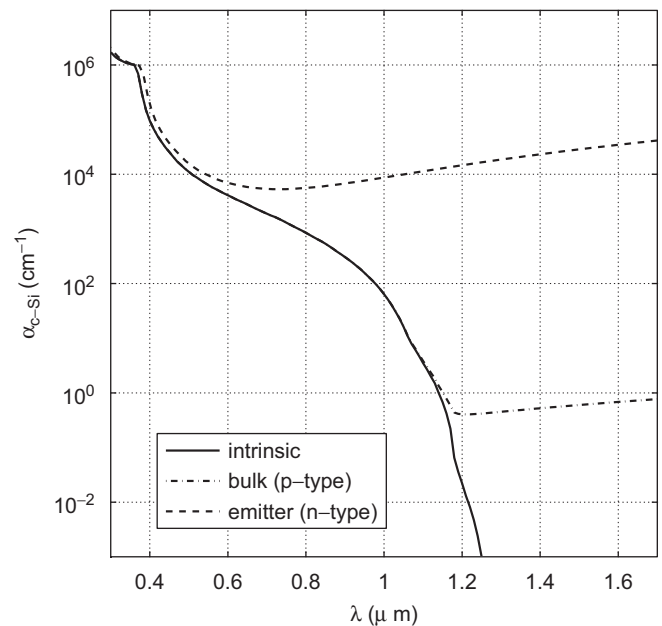


Fig. 2. The absorption coefficient of crystalline silicon as a function of wavelength for intrinsic silicon [17], p-type silicon with typical bulk doping concentration and n-type silicon with typical emitter doping concentration [5]. Doping concentration are given in the text.

absorption coefficient,

$$\alpha_{fc} = 2.6 \times 10^{-18} c_n \lambda^3 + 2.7 \times 10^{-18} c_p \lambda^2, \quad (4)$$

where α_{fc} is given in cm^{-1} , λ in μm and c_n and c_p in cm^{-3} .

The p-type doping concentration in the bulk of the wafer typically is $1.0 \times 10^{16} \text{cm}^{-3}$ and the maximum n-type doping concentration in the emitter typically is $3.3 \times 10^{20} \text{cm}^{-3}$ [18]. For these typical doping concentrations the absorption coefficient $\alpha_{c\text{-Si}}$ is illustrated in Fig. 2. By evaluation of the product of these absorption coefficients and the corresponding layer thickness, it is found that for $\lambda > 1.2 \mu\text{m}$ free-carrier absorption is dominant and hence this effect is taken into account.

2.2. The net-radiation method

A multi-layer configuration is a simple representation of a PV cell. For now the interfaces are assumed to be flat and smooth, so reflections are specular and the (unidirectional) net-radiation method [19] can be used to find A_λ . In this method at each interface y , four fluxes $q_{y,x}$ are defined where $x = a, b, c, d$ (see left panel of Fig. 3). Each flux contains the net-radiation, i.e. the contributions of multiple reflections between the interfaces. For each interface y , the following relationships exist between the net-radiation fluxes,

$$\begin{cases} q_{y,a} = \tau_{y-1} \cdot q_{y-1,d}, \\ q_{y,b} = r_y \cdot q_{y,a} + t_y \cdot q_{y,c}, \\ q_{y,c} = \tau_y \cdot q_{y+1,b}, \\ q_{y,d} = r_y \cdot q_{y,c} + t_y \cdot q_{y,a}, \end{cases} \quad (5)$$

where r_y is the intensity coefficient of reflection and $t_y = 1 - r_y$. These coefficients are determined using Fresnell's laws [20] in which the different polarization states are

treated separately. Further

$$\tau_y = e^{-\alpha_y d_y / \cos \phi_y}, \quad (6)$$

is the transmission coefficient of layer y and α_y and d_y are the layer's absorption coefficient and thickness, respectively. The distance irradiance travels in a single pass through layer y is given by $d_y / \cos \phi_y$, where ϕ_y is the propagation direction of irradiance in the layer, measured from the interface normal direction. No irradiance is incident from below so $q_{Y,c} = 0$, where Y indicates the final interface. Because all fluxes are proportional to $q_{1,a}$, it will be convenient to non-dimensionalize the fluxes, so that $q_{1,a} = 1$.

The unknown fluxes can be found by solving the set of linear equations (5) and the spectral absorption factor of layer y is given by,

$$A_{\lambda,y} = q_{y,d} - q_{y+1,a} + q_{y+1,b} - q_{y,c}. \quad (7)$$

By summing the spectral absorption factor of the individual layers, the spectral absorption factor of the entire multi-layer configuration is found,

$$A_\lambda = \sum_{y=1}^{Y-1} A_{\lambda,y}. \quad (8)$$

The spectral reflection and transmission factors are given by,

$$R_\lambda = q_{1,b}, \quad (9)$$

$$T_\lambda = q_{Y,d}, \quad (10)$$

and it can be checked that in this method energy is automatically conserved,

$$R_\lambda + A_\lambda + T_\lambda \equiv 1. \quad (11)$$

Net-radiation flux q contains contributions originating from multiple reflections and its intensity is assumed to be the sum of all contributions. This is only correct if no interference effects occur, i.e. if the optical thickness of each layer exceeds the coherence length of the irradiance being approximately $1 \mu\text{m}$ for solar irradiance [20]. In the c-Si PV cells considered here, this is true for all layers except for the AR coating, whose working principle is just based on the interference effect. Hence the effective reflection coefficient r_{ARC} of the AR coating is first calculated separately, taking into account the interference effect [21]. In the multi-layer system the coating is then represented as a single interface, characterized by r_{ARC} .

2.3. Light scattering at interfaces

The spectral absorption factor A_λ of weakly absorbed irradiance depends very much on the degree of optical confinement. If confinement is poor, a large part of the irradiance that has entered the cell will escape after a few passes, resulting in a low A_λ . However, irradiance scattered into oblique directions can be trapped inside the cell for many passes, increasing the pathlength and hence A_λ .

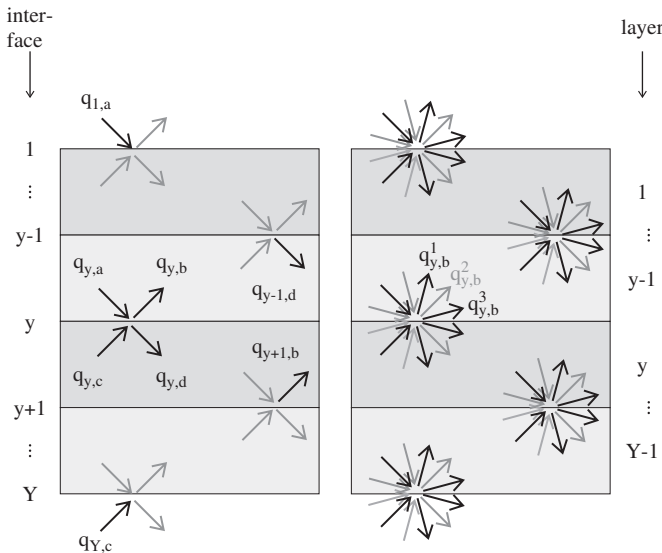


Fig. 3. A schematic overview of the fluxes defined at each interface in the net-radiation method. Left: the unidirectional model, as described in Section 2.2. Right: the multi-directional model, as described in Section 2.4.

In order to describe optical confinement correctly, light scattering at the interfaces has to be modeled as well.

The most general situation is illustrated in the left frame of Fig. 4. Consider irradiance incident on an interface with an angle θ_{in} . Both reflected and transmitted irradiance are scattered. The angular distribution of reflected irradiance over the angle of reflection θ_r and the distribution of transmitted irradiance over the angle of transmission θ_t are functions of θ_{in} . In literature both empirical and physical/optical scatter models can be found [22–24] which can determine the distribution of scattered irradiance for a given interface morphology. In principle any of these scatter models can be used.

For textured c-Si wafers considered in this paper, the dimensions of the texture features are larger than the wavelength of solar irradiance. This implies that the laws of geometrical optics apply and hence ray-tracing can be used to determine the angular distribution of scattered irradiance.

In the model the morphology of the textured interface is represented by a simple 2D periodic pattern, such as the parabolic pattern indicated in the right panel of Fig. 4. Effective steepness γ is a model parameter defined by,

$$\tan \gamma = h/w, \quad (12)$$

where h and w are the feature height and width, respectively. Besides the parabolic texture other 2D periodic texture profiles can be modeled and smooth interfaces are modeled by a ‘texture’ with zero steepness, i.e. $\gamma = 0^\circ$.

If the ray-traveling direction range from 0° (surface normal direction) to 90° (surface parallel direction) is divided into angular intervals, then the fraction of irradiance scattered into each of the intervals can be determined using the scatter model. In fact this can be done for different angles of incidence θ_{in} to construct interface matrices \mathbf{r} of which element r_{ij} contains the fraction of irradiance incident from interval i that is scattered into interval j . For each interface four different matrices exist: \mathbf{r}_+ , \mathbf{r}_- , \mathbf{t}_+ and \mathbf{t}_- , where r and t indicate reflected and

transmitted (refracted) irradiance and $+$ and $-$ indicate incident irradiance coming from above and below the interface. These interface matrices will be used in the so-called multi-directional net-radiation method, which takes into account scattering of irradiance.

2.4. The multi-directional net-radiation method

In order to incorporate the effect of irradiance scattered in multiple directions, the net-radiation method (described in Section 2.2) is extended. In the multi-directional net-radiation method fluxes are defined at each angular interval as schematically indicated in the right panel of Fig. 3. It is convenient to label the fluxes in the following way: $q_{y,x}^i$, where i is the angular interval number and again y is the interface number and $x = a, b, c, d$ and then to group them into vectors, e.g. $\mathbf{q}_{1,a} = (q_{1,a}^1, q_{1,a}^2, \dots)$.

The relationships between the net-radiation fluxes can be written compactly in terms of multiplications of flux-vectors and interface matrices,

$$\begin{cases} \mathbf{q}_{y,a} = \tau_{y-1} \cdot \mathbf{q}_{y-1,d}, \\ \mathbf{q}_{y,b} = \mathbf{r}_{y,+} \cdot \mathbf{q}_{y,a} + \mathbf{t}_{y,-} \cdot \mathbf{q}_{y,c}, \\ \mathbf{q}_{y,c} = \tau_y \cdot \mathbf{q}_{y+1,b}, \\ \mathbf{q}_{y,d} = \mathbf{r}_{y,-} \cdot \mathbf{q}_{y,c} + \mathbf{t}_{y,+} \cdot \mathbf{q}_{y,a}, \end{cases} \quad (13)$$

where for each interface y four matrices exist $\mathbf{r}_{y,+}$, $\mathbf{r}_{y,-}$, $\mathbf{t}_{y,+}$ and $\mathbf{t}_{y,-}$. The fifth matrix τ_y describes how irradiance is transmitted through a layer. Notice the similarity between Eqs. (5) and (13).

The unknown fluxes can be found by solving the set of linear equations (13) and the spectral absorption factor of layer y is given by,

$$A_{\lambda,y} = \sum_i (q_{y,d}^i - q_{y+1,a}^i + q_{y+1,b}^i - q_{y,c}^i), \quad (14)$$

where the sum is over all angular intervals i . The spectral absorption factor of the entire multi-layer configuration is again found by summing the spectral absorption factor of the individual layers. The hemispherical spectral reflection and transmission factors are given by,

$$R_\lambda = \sum_i q_{1,b}^i, \quad (15)$$

$$T_\lambda = \sum_i q_{Y,d}^i. \quad (16)$$

3. Reflection and transmission measurements

The spectral reflection factor R_λ and transmission factor T_λ were measured for a set of samples. In this section the experimental setup and the samples are briefly described and in Section 4 the measurements will be compared to the numerical results.

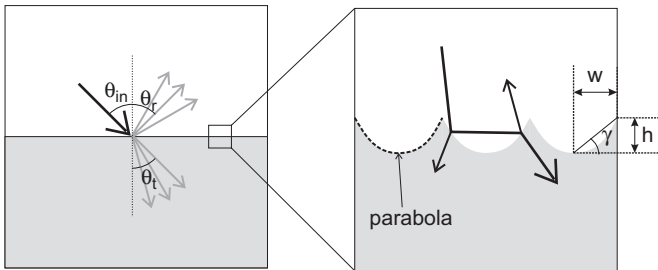


Fig. 4. Illustration of the scatter model. Left: Irradiance incident with an angle θ_{in} is scattered by the interface. Reflected and refracted irradiance are distributed over the angles θ_r and θ_t , respectively. Right: A detailed view of a textured interface, represented by a 2D periodic parabolic profile. Three periods are shown and steepness γ is indicated.

3.1. Experimental set-up

To measure the hemispherical reflectance R_λ of a sample, a Labsphere RTC 060 SF integrating sphere is used which collects the reflected irradiance scattered in all hemispherical directions. The intensity inside the Spectrafect® coated sphere is proportional to R_λ and is measured by an Instruments Systems spectroradiometer (Spectro 320 R5). Using this setup, besides the hemispherical reflectance R , the hemispherical transmittance T can be determined with a 1% inaccuracy for $0.33 < \lambda < 1.4 \mu\text{m}$.

3.2. Samples

A complete c-Si PV cell is a complex optical device in which several optical effects occur simultaneously. In order to validate the model a set of samples was prepared with a gradually increasing complexity. In this way one optical effect is introduced at the time and it can be checked whether this effect is captured by the model. Next a brief description of samples 1–5 is given and the details are given in Table 1.

All samples are c-Si wafers and have a p-type boron bulk doping concentration of $1.0 \times 10^{16} \text{ cm}^{-3}$, resulting in a resistivity of $1.5 \Omega \text{ cm}$. Sample 1 is a reference sample of Czochralski (cz) mono-crystalline silicon of $500 \mu\text{m}$ thickness. Both sides are polished to flat and smooth interfaces. Samples 2–5 are multi-crystalline (mc) silicon textured wafers of approximately $300 \mu\text{m}$ thickness. They are textured by means of an acid texture etch, resulting in a pitted surface [25] at the front and to a lesser extent also at the back.

Samples 3–5 have a phosphorous emitter of $62 \Omega \square$. Details of the emitter will be given in Section 4.3. Samples 4 and 5 have a standard plasma enhanced chemical vapor deposition (PECVD) silicon-nitride (Si_3N_4) AR coating with a thickness of typically 80 nm . Sample 5 has a standard aluminium back contact, which was screen-printed on the backside of the wafer and then alloyed.

4. Results

In this section the numerical and experimental results are compared. This is done for the samples given in Table 1.

Table 1
Crystalline silicon samples 1–5

Nr	Material	Thickness (μm)	Interface	Emitter	ARC	Back contact
1	cz Si	500	Polished	–	–	–
2	mc Si	325	Textured	–	–	–
3	mc Si	318	Textured	$62 \Omega \square$	–	–
4	mc Si	309	Textured	$62 \Omega \square$	Yes	–
5	mc Si	325	Textured	$62 \Omega \square$	Yes	Al alloyed

cz = Czochralski mono-crystalline, mc = multi-crystalline.

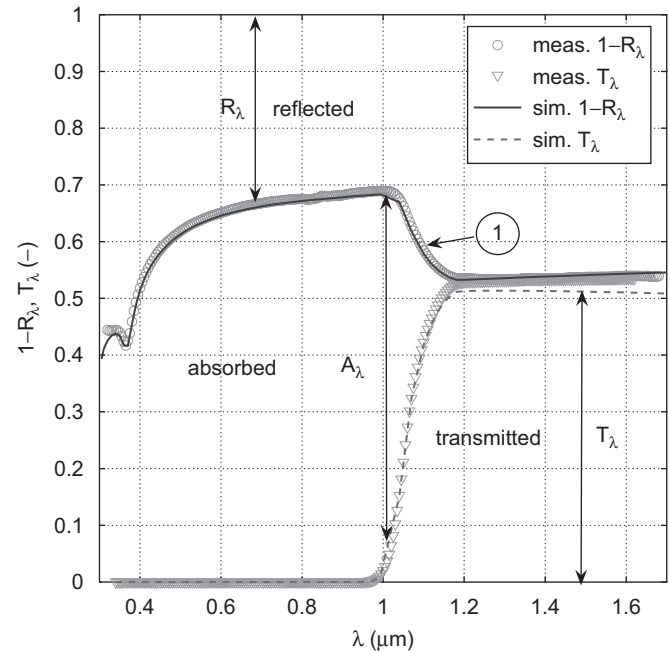


Fig. 5. Measured and simulated $1 - R_\lambda$ and T_λ as a function of λ for a polished wafer (sample 1).

In the following figures $1 - R_\lambda$ and T_λ are plotted so the area in between corresponds to the spectral absorption factor $A_\lambda = 1 - R_\lambda - T_\lambda$. The numerical results are plotted in the same way. Measurement results are indicated by symbols (\circ , ∇) and numerical results by lines.

4.1. Polished wafer

In Fig. 5 the results are shown for sample 1, the double sided polished wafer. This measurement illustrates that for $\lambda < 1.0 \mu\text{m}$ the wafer is opaque ($T_\lambda = 0$) while for $\lambda > 1.2 \mu\text{m}$ the wafer is transparent ($A_\lambda \approx 0$). The increase in R_λ for $\lambda > 1.2 \mu\text{m}$ (indicated by arrow 1) is caused by the transparency of the wafer, allowing irradiance to be internally reflected by the back interface. Both front and back surface were modeled as smooth interfaces. As can be seen the numerical results agree very well with the experiments.

4.2. Textured wafer

When the measurement results of the textured sample 2 (Fig. 6) are compared to the previous sample, the two advantages of texture can be seen. Firstly, in the opaque regime ($\lambda < 1.0 \mu\text{m}$) R_λ is reduced as a result of improved incoupling (indicated by arrow 2). Secondly, in the transparent regime ($\lambda > 1.2 \mu\text{m}$) A_λ has increased (indicated by arrow 3) as a result of the increased pathlength caused by the improved optical confinement.

As described in Section 2.3, textured interfaces are modeled as a parabolic profile and by numerically varying the profile steepness γ , the amount of incoupling and hence the ‘effective’ reflection coefficient of the textured interface

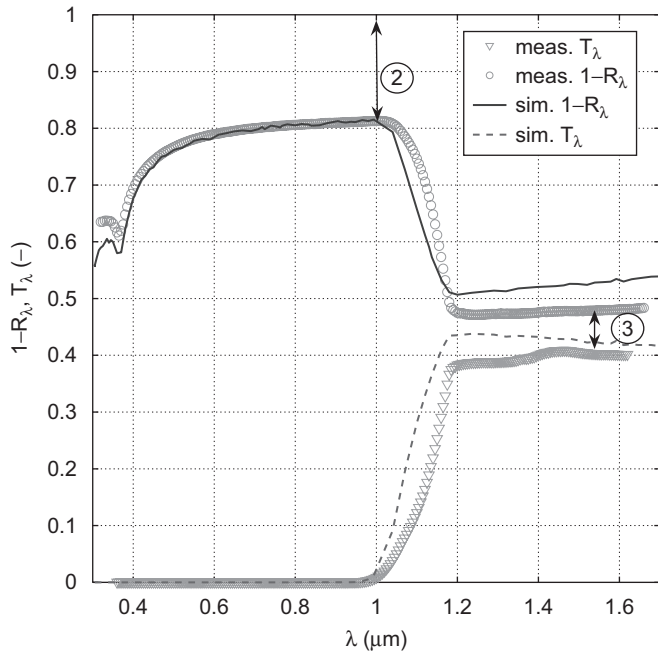


Fig. 6. Measured and simulated $1 - R_\lambda$ and T_λ as a function of λ for a textured wafer (sample 2).

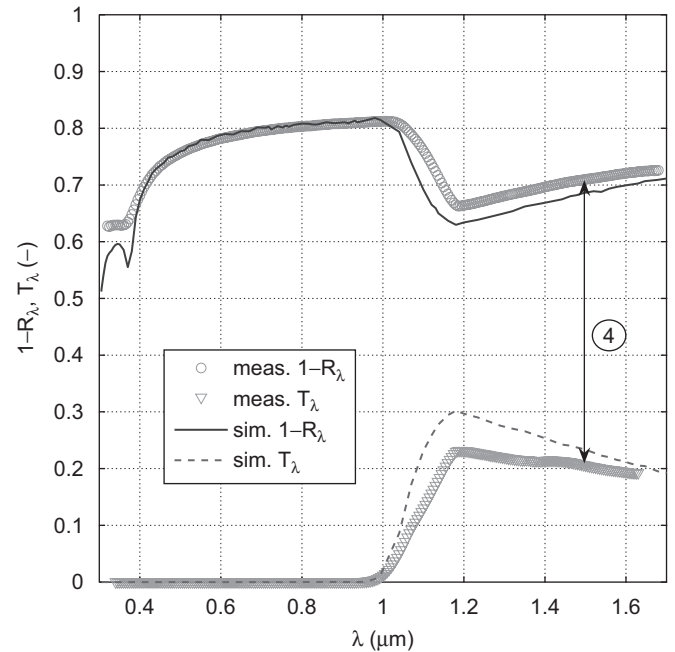


Fig. 7. Measured and simulated $1 - R_\lambda$ and T_λ as a function of λ for a textured wafer with emitter (sample 3).

can be controlled. By comparing the measured values of $R_{\lambda=1.0 \mu\text{m}}$ for both the front and the backside of the textured wafer to the results of a ray-tracing analysis it was found that a texture steepness of 41° and 32° are required for the front and the back, respectively. Hence $\gamma_{\text{front}} = 41^\circ$ and $\gamma_{\text{back}} = 32^\circ$ will be used to model the front and back interfaces of all textured wafers (samples 2–5). The small deviation for $\lambda > 1.0 \mu\text{m}$ is discussed in the next section.

It can be seen that both the reduction of $R_{\lambda < 1.0 \mu\text{m}}$ and the increase of $A_{\lambda > 1.2 \mu\text{m}}$ are also found numerically. This means that the parabolic profile, besides the incoupling effect, also captures the scattering and trapping effect quite well. Note that the parabolic profile was used because it best resembles the pitted profile of an acid etch textured wafer surface. If texture is represented by a different profile, such as a zigzag profile, then there is less agreement between model and measurement. This indicates that besides the steepness, the shape of the texture profile is important as well.

4.3. Emitter

Sample 3 is identical to the previous one with a phosphorous emitter with a sheet resistance of $62 \Omega/\square$ added. The Hall-effect is commonly exploited to determine the electrically active doping concentration. Bisschop [18] has determined the doping profile $c(z)$ of similar emitters using stripping Hall measurements, where z is the distance to the wafer front. The emitter profiles have a maximum doping concentration $c(0) = 3.3 \times 10^{20} \text{ cm}^{-3}$ at the surface and their areal doping concentration $C = \int c(z) dz = 1.8 \times 10^{15} \text{ cm}^{-2}$.

From the optical measurement results (Fig. 7) it can be seen that for $\lambda < 1.0 \mu\text{m}$ there is no difference with the previous sample. However, for $\lambda > 1.2 \mu\text{m}$, A_λ has increased tremendously because of free-carrier absorption in the emitter (indicated by arrow 4). Note that though this absorption mechanism increases the AM1.5 absorption factor significantly, the electrical efficiency is hardly affected, since no additional electron–hole pairs are generated.

Since the free-carrier absorption coefficient is linear in doping concentrations c_n (c_p), the amount of free-carrier absorption only depends on the areal doping concentration C . Hence the emitter was modeled as a single layer with a constant doping concentration equal to peak concentration $c_n(0)$ and an effective thickness $d = C/c_n(0) = 55 \text{ nm}$.

Similar to the experiments, the model results show that the addition of an emitter results in a large increase in $A_{\lambda > 1.2 \mu\text{m}}$ (Fig. 7).

4.4. AR coating

Sample 4 is identical to the previous one, only an AR coating was added to the front. From the experimental results (Fig. 8) it can be seen that for $\lambda \approx 0.7 \mu\text{m}$ the coating reduces R_λ to very low values (indicated by arrow 5). This is a well known interference effect exploited by AR coatings. This effect is modeled with a coating thickness of 84 nm and good agreement is found. There is a small deviation for $\lambda = 0.4 \mu\text{m}$ (indicated by arrow 6) which would disappear if a slightly higher optical absorption

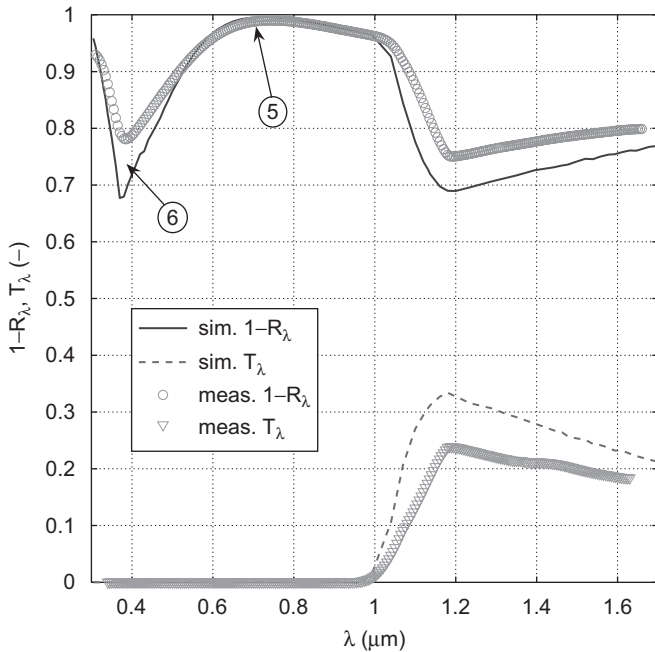


Fig. 8. Measured and simulated $1 - R_\lambda$ and T_λ as a function of λ for a textured wafer with emitter and AR coating (sample 4).

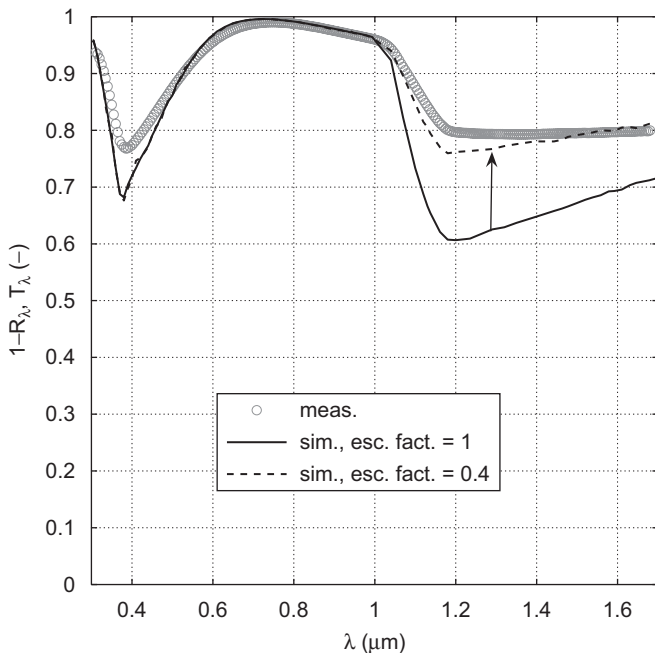


Fig. 9. Measured and simulated $1 - R_\lambda$ as a function of λ for a textured wafer with emitter, AR coating and back contact (sample 5). The solid line represents a simulation without correction (i.e. with an escape factor of 1) and the dashed line represents a corrected simulation with an escape factor of 0.4.

in the Si_3N_4 coating is assumed. It is known that for $\lambda < 0.4 \mu\text{m}$ there can be some absorption in the coating and the exact amount depends on the deposition conditions [26].

4.5. Back contact

Sample 5 is similar to the previous sample, but with an aluminium back contact. This back contact is opaque, so $T_\lambda = 0$ and only $A_\lambda = 1 - R_\lambda$ is shown in Fig. 9. Irradiance with $\lambda < 1.0 \mu\text{m}$ does not reach the back contact, so that part of the graph is similar to the graph of the previous sample without back contact. However, irradiance with $\lambda > 1.2 \mu\text{m}$ is mostly reflected by the back contact and, if it escapes the wafer at the front, it reduces $A_\lambda > 1.2 \mu\text{m}$.

The model result (solid line) gives a somewhat lower $A_\lambda > 1.2 \mu\text{m}$ compared to the measurement, i.e. the model overpredicts the amount of escaping irradiance. In order to correct this, the chance that trapped irradiance escapes the wafer was numerically reduced to 40% of the original value, i.e. an escape factor of 0.40 is used. This escape factor points out to be necessary to take into account 3D effects occurring for trapped irradiance. In Appendix A an explanation is given and the value of 0.40 is made plausible. The results are shown in Fig. 9 (dashed line). As can be seen a very good agreement is found with the experimental results over the entire wavelength range.

4.6. Encapsulation

c-Si cells in a PV panel are encapsulated in the following way: glass/EVA/cell/EVA/tedlar®/polyester/tedlar®, where EVA stands for ethyl vinyl acetate and special low iron content glass is used. The presence of encapsulation allows irradiance to be trapped inside the glass layer. An extra simulation was performed to investigate the overall effect of the encapsulation. The simulated configuration,

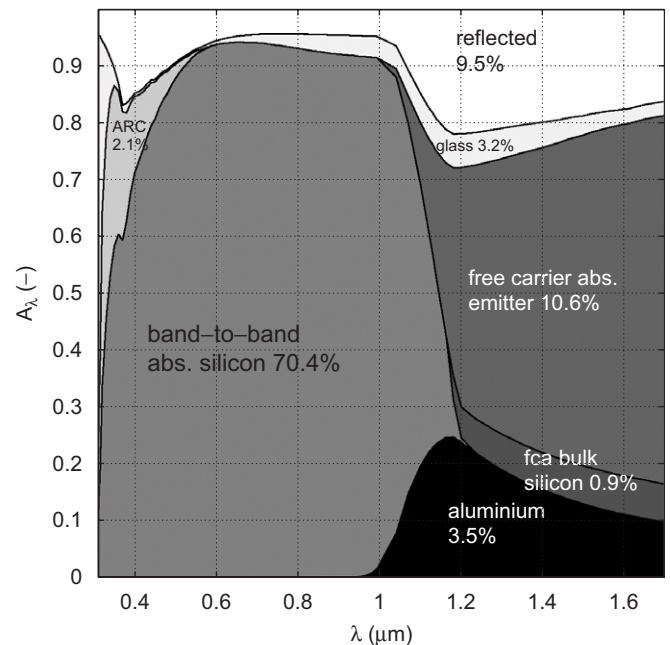


Fig. 10. Area plot of the spectral absorption factor A_λ for each layer of configuration 6. The AM1.5 absorption factors are also given for each layer separately. The total absorption factor is 90.5%.

denoted as configuration 6, has a 3 mm thick low iron content glass cover added. It is assumed that the optical properties of EVA are similar to those of glass and hence the EVA layer was not modeled separately.

The results are shown in Fig. 10. The spectral absorption factor is indicated for each layer separately. The remaining white area represents R_{λ} . It can be seen that for short-wavelength solar irradiance ($\lambda < 1.1 \mu\text{m}$) the band-to-band absorption is dominant, while for long-wavelength solar irradiance free-carrier absorption in the emitter is dominant. Smaller fractions of the AM1.5 spectrum are absorbed in the glass cover, in the AR coating and in the back contact.

4.7. Comparison of experimental and numerical results

In Table 2 an overview is given of the performed simulations. The simulated absorption factors are compared to the ones derived from the experiments on samples 1–5. It can be seen that the absorption factor of a bare polished wafer (sample 1) is only 49.5%. Because of reduction of reflective losses by texture and AR coating and by absorption in emitter and back contact this increases to as much as 90.2% for an almost complete cell (sample 5).

The numerical model is completely based on the laws of (geometrical) optics. Only the texture steepness γ is used as parameter to fit the amount of incoupling of irradiance for $\lambda > 1.0 \mu\text{m}$ to the measured values. For $\lambda > 1.0 \mu\text{m}$ trapping of irradiance inside the wafer is an important effect, which has essentially a three-dimensional (3D) nature while the model is 2D. But even without correcting for 3D effects in light trapping, the deviations in AM1.5 absorption factor A from the experimental values are at most 3.6%. After compensating for the 3D effects by means of an escape factor, the deviation is even reduced to only 1.2%. The remaining deviation originates mainly from the blue part of the solar spectrum ($\lambda \approx 0.4 \mu\text{m}$) and is caused by some extra absorption in the AR coating, not taken into account by the model.

The effect of encapsulation was only investigated numerically (configuration 6). By comparing the absorption factors for configurations 5 and 6 it can be seen that

Table 2
The numerical and the corresponding measured AM1.5 absorption factor A

Nr	Description	A_{num} (%)	A_{exp} (%)
1	Bare polished c-Si wafer	49.9	49.5
2	+ Texture (acid etch)	63.4	64.1
3	+ Emitter ($62 \Omega_{\square}$)	69.7	71.4
4	+ AR coating (Si_3N_4)	82.3	85.8
5	+ Back contact (Al)	86.6 89.0*	90.2
6	+ Encapsulation	90.5*	–

For numerical results marked with *, an escape factor of 0.4 was used.

encapsulation increases the absorption factor from 89.0% to 90.5%. This encapsulated configuration will be used as reference configuration in Section 5.

5. Influence of the cell design

The influence of the cell design on the absorption factor will be investigated using the numerical model in Sections 5.1–5.4, e.g. by varying the steepness of the texture, the strength of the emitter and the reflection coefficient of the back contact. Each time configuration 6, which has encapsulation and an escape factor of 0.4, will be used as a starting point. This information will be used in Sections 5.5 and 5.6, where the effect of the absorption factor on the *annual* electrical yield of PV systems and both the annual electrical and thermal yield of PVT systems is discussed.

5.1. Texture steepness

First the steepness γ of the texture at the front of the silicon wafer is numerically varied. Note that γ defined by Eq. (12) is an ‘average’ steepness and that for the parabolic profile the local steepness varies from point to point. The results are shown in Fig. 11 (solid line). If no texture is present ($\gamma = 0^\circ$), reflective losses are high, resulting in an AM1.5 absorption factor of only 86.5%. However, if texture steepness γ increases to above 8° , A starts to increase. This is caused by irradiance being trapped inside the glass cover [25]. Irradiance reflected by sufficiently steep texture is reflected back onto the glass cover front surface outside the critical angle. Hence this irradiance is

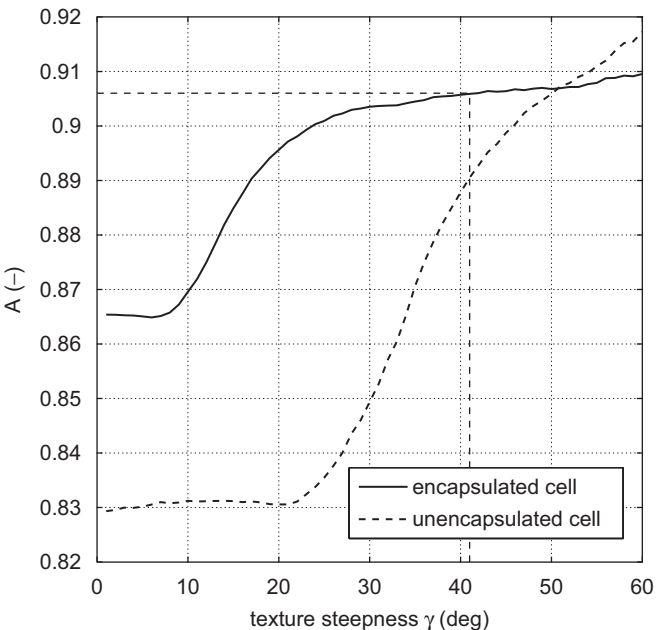


Fig. 11. The AM1.5 absorption factor A as a function of the steepness γ of the texture at the front of the c-Si wafer for both an encapsulated and unencapsulated configuration (configurations 6 and 5).

totally internally reflected back into the forward direction. This guarantees incident irradiance at least two chances of entering the wafer before any chance of escaping the glass arises. Hence for a texture steepness of $8\text{--}25^\circ$ there is a strong increase in A to above 90%. Further increasing the steepness to more than 25° only results in a small increase in A . This is in contrast with an unencapsulated cell, which has no glass cover to trap reflected irradiance. As a result the absorption factor remains low up to $\gamma = 25^\circ$ and then increases sharply, shown as the dashed line in Fig. 11.

5.2. Emitter strength

Since a significant part of long-wavelength irradiance is absorbed by free-carrier absorption in the emitter, the effect of emitter strength on the AM1.5 absorption factor A is investigated. By varying the emitter thickness, the areal (integral) doping concentration and hence the corresponding sheet resistance can be varied. In Fig. 12 the absorption factor A is shown as a function of sheet resistance. In case the emitter is omitted, the AM1.5 absorption factor is 86.1%. A typical emitter increases this to between 90.2% (at $80\Omega_{\square}$) and to 91.2% (at $40\Omega_{\square}$).

5.3. Back contact reflectivity

Also the effect of back contact reflectivity on absorption factor A is investigated. Note that only long-wavelength solar irradiance ($\lambda > 1.0\mu\text{m}$) reaches the back contact and can be affected by it. The value of r_{back} is numerically varied between 0 and 1, i.e. between a perfectly absorbing and a perfectly reflecting back contact. The results are shown in Fig. 13. It can be seen that A varies between

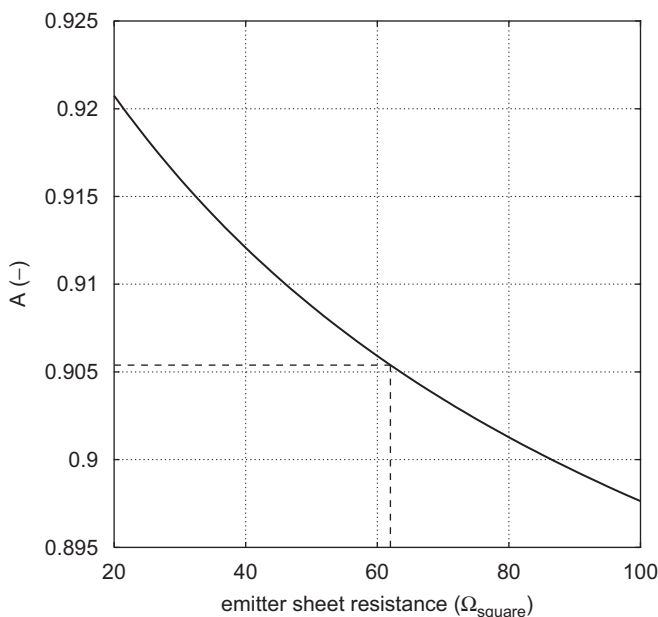


Fig. 12. The AM1.5 absorption factor A as a function of emitter sheet resistance for an encapsulated configuration (configuration 6).

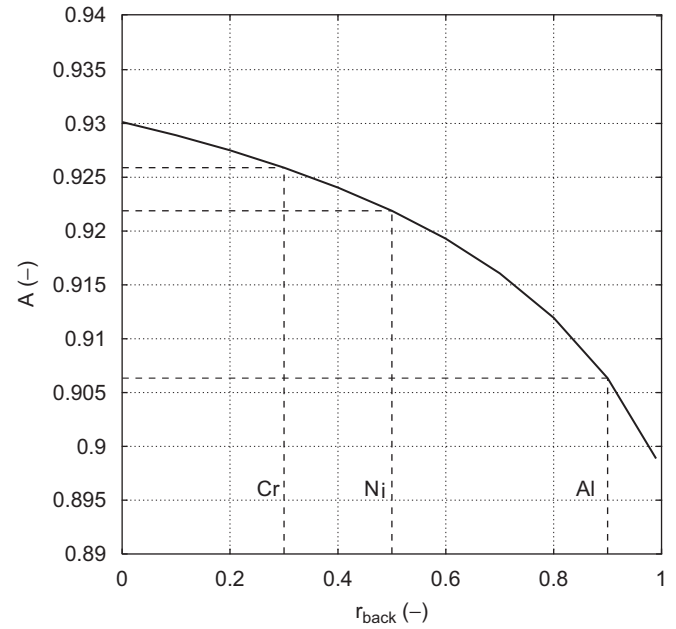


Fig. 13. The AM1.5 absorption factor A as a function of back contact reflectance r_{back} for an encapsulated configuration (configuration 6).

89.9% and 93.0%. The higher value corresponds to a perfectly absorbing back contact.

The aluminium back contact used in the reference configuration is very reflective, i.e. $r_{\text{back}} \approx 0.90$. One could consider to use nickel (Ni) or chromium (Cr) instead of aluminium (Al) as a back contact. Both from reflection measurements carried out on a number of additional samples and from the Fresnel relations it follows that with a Ni back contact $r_{\text{back}} \approx 0.50$ and with a Cr back contact $r_{\text{back}} \approx 0.30$. From the results it can be derived that an encapsulated PV cell with a nickel or chromium back contact would have an absorption factor as high as 92.3% or 92.7%, respectively. A consequence of the use of less reflecting back contact materials is that the PV efficiency will drop by approximately 0.3% absolute. This drop is caused by the absorption of near bandgap solar irradiance which, if absorbed in the back contact, can no longer generate photocurrent.

5.4. Metal coverage of front contact

Up till now only the active cell area was considered. However, a part of the PV cell can be covered by the front contact grid. So in order to determine the absorption factor of the entire PV cell (A_{cell}) a weighted average is taken of the active (ac) area absorption factor and the front contact grid (gr) area absorption factors,

$$A_{\text{cell}} = a_{\text{ac}}A_{\text{ac}} + a_{\text{gr}}A_{\text{gr}}, \quad (17)$$

where A is the absorption factor and a is the relative surface area. Here the absorption factor of the standard configuration (configuration 6) is taken as active area absorption factor, i.e. $A_{\text{ac}} = 90.5\%$. The spectral absorption

Table 3

The relative active area a_{ac} and grid area a_{gr} for different c-Si cell concepts and the resulting cell absorption factor A_{cell}

	H-pattern	PUM	EWT
$A_{ac} = 90.5\%$, $A_{gr} = 22.7\%$,	$a_{ac} =$ $a_{gr} =$	0.920 0.080	0.955 0.045
$A_{cell} (%)$	85.1	87.4	90.5

Table 4

The absorption factor and electrical efficiency of four cell designs and the resulting relative temperature loss δ , if these cell would be applied in a PV array or in a PVT system

	H-pattern planar	H-pattern textured	PUM textured	EWT textured
$A_{cell} (%)$	81.4	85.1	87.4	90.5
$\eta_{el}^{STC} (%)$	14.4	15.0	15.6	16.1
$A_{eff} (%)$	67.0	70.1	71.8	74.4
<i>Applied in a PV array</i>				
$\delta (%)$	−8.2	−8.5	−8.8	−9.1
$\bar{\eta}_{el}^T (%)$	13.2	13.7	14.2	14.6
<i>Applied in a PVT system</i>				
$\delta (%)$	−14.4	−15.1	−15.4	−16.0
$\bar{\eta}_{el}^T (%)$	12.3	12.7	13.2	13.5
$\eta_{th} (%)$	24.0	25.0	25.5	26.2

factor of the screen printed silver front metallization was measured [27]. By integrating these results over the solar spectrum, it was found that $A_{gr} = 22.7\%$. In case of a standard H-pattern grid, i.e. parallel fingers connected by two or three busbars, the relative grid area a_{gr} is approximately 8.0%. As a result A_{cell} is reduced to 85.1%.

In pin-up module (PUM) cells [28] the surface area of the front grid is reduced. In these cells current is fed through a limited number of holes in the cell and collected at the back of the cells and no busbars are required. Since the grid coverage is reduced A_{cell} is increased to 87.4%. Alternatively, emitter wrap through (EWT) cells [29] can be used in which the emitter is fed through the wafer at a large number of spots. Since no metal front grid is required, $A_{cell} = A_{ac} = 90.5\%$. An overview is given in Table 3.

5.5. Effect of absorption factor on electrical yield of PV systems

In the previous sections the influence of cell design on the absorption factor was investigated, here the effect of the absorption factor on the annual electrical yield is discussed. This will be done using the four cell designs given in Table 4. The first cell is planar, i.e. untextured, and has a H-pattern contact grid. The other three cells are the textured cells already introduced in Section 5.4. The absorption factor of these cells A_{cell} and their electrical

efficiency at standard test conditions η_{el}^{STC} were determined using the optical model described in Section 2 and PV device model PC1D [9].

Absorbed irradiance is either converted into heat or electricity. Hence the amount of heat generated in an operational PV cell is proportional to the effective absorption factor,

$$A_{eff} = A_{cell} - \eta_{el}, \quad (18)$$

where η_{el} is the electrical efficiency.

The effective absorption factor is also indicated in Table 4 and it can be seen that cells which absorb most solar irradiance have the highest electrical efficiency, but also have the highest A_{eff} , i.e. they produce most heat.

PV cells applied in free-standing or roof-integrated systems will reach temperatures well above the ambient temperature. The difference between cell and ambient temperature is approximately proportional to the amount of heat absorbed per unit surface area,

$$T_{cell} - T_{amb} = \kappa A_{eff} G, \quad (19)$$

where G is the irradiance and proportionality constant κ for a free-standing array is approximately $0.043^\circ\text{C}/(\text{W}/\text{m}^2)$. Here κ is found by identifying the product κA_{eff} with $K = 0.03^\circ\text{C}/(\text{W}/\text{m}^2)$ found in literature [1] and assuming that $A_{eff} \approx 70\%$ is incorporated in this value (see also Table 4).

It is well known that an increase in cell temperature reduces the electrical efficiency of PV cells,

$$\eta_{el}(T_{cell}) = \eta_{el}^{STC} \{1 + \beta(T_{cell} - 25^\circ\text{C})\}, \quad (20)$$

where for c-Si cells temperature coefficient $\beta = -0.45\%/^\circ\text{C}$ [1]. An annual electrical efficiency $\bar{\eta}_{el}^T$ is introduced, containing a correction for the elevated cell temperatures,

$$\bar{\eta}_{el}^T = \eta_{el}^{STC} (1 + \delta), \quad (21)$$

where δ represents the relative reduction of the STC efficiency due to the temperature rise of the cells under operational conditions with respect to the ambient temperature. δ can be calculated using Eqs. (19)–(20) and the distribution of irradiance over the various irradiance classes during a year. It turns out that,

$$\delta = \beta \kappa A_{eff} \bar{G}, \quad (22)$$

where \bar{G} is the averaged irradiance, being $480 \text{ W}/\text{m}^2$ for central Europe (50° latitude) [10] and $630 \text{ W}/\text{m}^2$ for southern Europe (38° latitude) [30]. Assuming southern European irradiance levels, both δ and the corrected efficiency $\bar{\eta}_{el}^T$ are given in Table 4. It can be seen that, in the case of the cells investigated here, the cells with the highest η_{el}^{STC} also have the highest relative temperature loss δ , but the increase of this loss is only 0.9% comparing the case of planar H-patterned cells with EWT cells.

5.6. Effect of absorption factor on electrical and thermal yield of PVT systems

The approximation that was made for PV systems is not applicable to PVT systems. In these systems a collector loop transports heat from PV cells to a storage tank, from which heat can be extracted by a load. Hence the actual rise in cell temperature above the ambient temperature is not only a function of the actual irradiance, but also of the storage tank temperature.

The influence of the absorption factor on both the electrical and thermal yield of PVT systems was investigated using the model of Zondag [4]. In this case a PVT system located in central Europe (50° latitude) is considered with 6 m² PVT sheet-and-tube covered collectors and a 200 l storage tank. In Table 4 the relative temperature loss δ is given for each type of cell when applied in this PVT system. Again the relative temperature losses δ are higher for the cells with the highest $\eta_{\text{el}}^{\text{STC}}$.

Besides electricity PVT systems supply heat and in Table 4 the annual thermal system efficiency is given for each type of PV cell. It can be seen that because high efficiency cells produce more heat, they also give rise to higher thermal efficiencies. Note that because this PVT system during a large part of the year is operated at high tank temperatures, the temperature loss δ is relatively high and the thermal efficiency is relatively low.

The EWT cell ($\eta_{\text{el}}^{\text{STC}} = 16.1\%$) has an 11.8% relative higher $\eta_{\text{el}}^{\text{STC}}$ compared to the planar cell with H-pattern ($\eta_{\text{el}}^{\text{STC}} = 14.4\%$). Having taken into account the increase of the effective absorption factor, the temperature corrected $\bar{\eta}_{\text{el}}^T$ is 9.8% relative higher, implying that only 2.0% relative of the gain at STC is lost because of the higher cell temperatures. However, the gain in thermal efficiency of the PVT systems is significant: 9.2% relative (from 24.0% to 26.2%).

6. Conclusion

The absorption factor of a PV cell is the fraction of incident solar irradiance that is absorbed. This absorption factor is derived from spectral reflection and transmission measurements for a set of c-Si samples. The fact that texture and AR coating reduce reflective losses and increase the absorption factor was expected. However the effect of free-carrier absorption, especially in the emitter, on the absorption factor is unexpectedly large.

A 2D numerical model for the absorption factor of PV cells is developed, which is completely based on the laws of geometrical optics. The texture steepness parameter is used to describe incoupling of irradiance into textured cells. A so-called escape factor is incorporated into the model to take into account the 3D effect of trapping weakly absorbed solar irradiance.

When the numerical results are compared to the spectral measurements it was found that the effects of wafer texture, AR coating and free-carrier absorption are captured by the

model very well. It was shown numerically that the effect of texture steepness on the absorption factor very much depends on the presence of encapsulation. For an encapsulated cell a relatively moderate steepness of 20–30° is already sufficient to obtain a high absorption factor.

Different cell designs were considered to illustrate that in many cases an increase of the electrical efficiency is accompanied by an increase of the effective absorption factor and hence by an increase in the relative temperature loss. As an example a classical planar H-patterned cell is compared to a modern textured EWT cell. When considering the electrical efficiency at standard test conditions, the EWT cell outperforms the H-patterned cell by 11.8% relative. When considering the annual electrical yield and taking into account the elevated cell temperatures, this number is reduced by only 1.0% for cells applied in a PV array and by only 2.0% for cells applied in a PVT system. Note that in a PVT system the reduction in electrical yield is more than compensated by an increase of 9.2% relative in thermal yield.

Acknowledgements

The authors would like to thank Arthur Weeber, Valentin Mihailetchi and Martien Koppes of the Solar Energy Department of Energy Research Center, the Netherlands (ECN) for preparing sample wafers and assistance with the optical experiments. Herbert Zondag of ECN is acknowledged for critically reading the manuscript. This work was funded by Energy Research Centre of the Netherlands and by SenterNOVEM.

Appendix A. 3D effects in light trapping

The numerical model is 2D in the sense that a 2D cross-section of a multi-layer is considered. Almost every optical effect that occurs in real PV cells can be captured by a 2D model. However, for irradiance scattered by the back contact and returning to the textured silicon/air (or silicon/glass) interface, the 2D and 3D situation are different with respect to the fraction of irradiance that is transmitted by the interface and escapes the silicon wafer. A ray can only escape if it is inside the loss-cone. Unlike in a real 3D

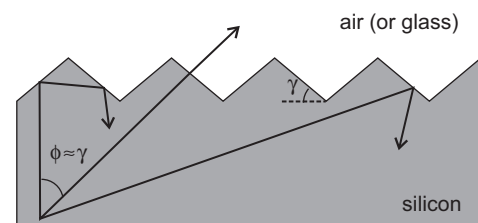


Fig. A.1. Three rays reflected by the back contact under different zenith angles ϕ , reaching the textured front of the wafer. Only the ray having a zenith angle close to the texture steepness, i.e. deviating less than the critical angle, has a chance of escaping.

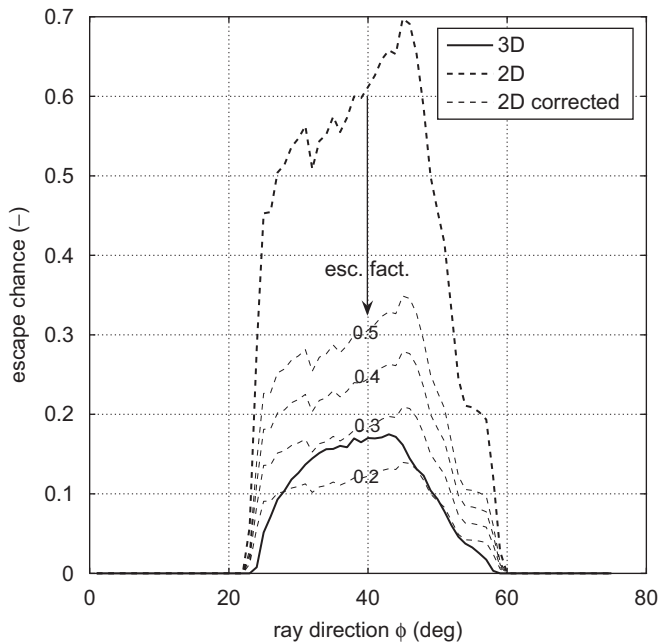


Fig. A.2. The escape chance as a function the ray's initial zenith angle ϕ , for a 3D situation (solid line) and a 2D situation with various escape factors (dashed lines).

situation, in a 2D model the loss-'cone' and the ray are always in the same plane, resulting in an overestimation of the chance of escape.

This effect was analysed by comparing the chance of escape through a textured silicon/air interface in both a 2D and 3D model. The situation is kept as simple as possible, i.e. the interface is characterized by fixed refractive indices at both sides ($N_{\text{Si}} = 3.42$ and $N_{\text{air}} = 1$) and a zigzag (2D) or pyramid (3D) texture with a steepness of 41° . Rays incident on the textured interface are released at a random point below the interface, with a random azimuth but under a well defined zenith angle ϕ (i.e. angle with the vertical direction, see Fig. A.1). The fraction of rays that is transmitted by the interface and can escape is analysed.

In Fig. A.2 the escape chance is plotted as a function of the ray's initial zenith angle ϕ . It can be seen that the 2D model (dashed line) and the 3D model (solid line) agree on the part of the angular domain for which total internal reflectance occurs, i.e. having an escape chance of zero. However, as expected, for the rest of the domain the 2D escape chance is much higher than the 3D escape chance. To incorporate this 3D effect in the 2D model an escape factor is introduced which reduces the escape chance. Note that this correction is only used for a relatively small amount of long-wavelength irradiance reaching to the front interface from the inside, e.g. after being reflected by the back contact.

References

[1] M.A. Green, *Solar-Cells-Operating Principles, Technology and System Applications*, Prentice-Hall, USA, 1982.

[2] W.G.J. van Helden, et al., PV thermal systems: PV panels supplying renewable electricity and heat, *Progr. Photovoltaics* 12 (2004) 415.

[3] PVT Roadmap, A European guide for the development and market introduction of PV-thermal technology, (www.pvtforum.org).

[4] H.A. Zondag, The thermal and electrical yield of a PV-thermal collector, *Solar Energy* 72 (2002) 113.

[5] M.A. Green, *Silicon Solar Cells: Advanced Principles & Practice*, University of New South Wales, Sydney, Australia, 1995, pp. 46–48.

[6] S. Krauter, R. Hanitsch, Actual optical and thermal performance of PV-modules, *Solar Energy Materials Solar Cells* 41/42 (1996) 557.

[7] N. Fraidenraich, O.C. Vilela, Exact solutions for multilayer optical structures, applications to PV modules, *Solar Energy* 69 (2000) 357.

[8] Z.H. Lu, Q. Yao, Energy analysis of silicon solar cell modules based on an optical model for arbitrary layers, *Solar Energy* 81 (2007) 636.

[9] D.A. Clugston, PC1D Version 5: 32-bit solar cell modeling on personal computers, in: 26th IEEE Photovoltaic Specialist Conference, Anaheim, 1997.

[10] C.W.A. Baltus, et al., Analytical monitoring of losses in PV systems, in: *Proceedings of the 14th European Solar Energy Conference*, 1997, pp. 1547–1550.

[11] H.A. Zondag, The yield of different combined PV-thermal collector designs, *Solar Energy* 74 (2003) 253.

[12] S.A. Kalogirou, et al., Hybrid PV/T solar systems for domestic hot water and electricity production, *Energy Conversion Management* 47 (18–19) (2006) 3368.

[13] S.A. Kalogirou, et al., Industrial application of PV/T solar energy systems, *Appl. Thermal Eng.* 27 (8–9) (2007) 1259.

[14] R. Hulstrom, et al., Spectral solar irradiance data sets for selected terrestrial conditions, *Solar Cells* 15 (1985) 365.

[15] E.D. Palik, *Handbook of Optical Constants of Solids*, 1985, pp. 397–401.

[16] M. Rubin, Soda lime silica glasses, *Solar Energy Materials* 12 (1985) 275.

[17] M.A. Green, et al., Optical properties of intrinsic silicon at 300 K, *Progr. Photovoltaics* 3 (1995) 189.

[18] F. Bisschop, Characterization and modeling of highly doped regions in silicon solar cells, Ph.D. Thesis, University Utrecht, The Netherlands, 1992.

[19] R. Siegel, The net-radiation method for transmission through partially transparent plates, *Solar Energy* 15 (1973) 273.

[20] E. Hecht, *Optics*, fourth ed., Addison-Wesley, Reading, MA, 2004, p. 111.

[21] H.A. Macleod, *Thin-film Optical Filters*, second ed., Adam Hilger Ltd., Bristol, UK, 1986, pp. 11–45.

[22] B.T. Phong, Illumination for computer generated pictures, *Commun. ACM* 18 (1975) 311.

[23] R. Brendel, SUNRAYS: a versatile ray tracing program for the photovoltaic community, in: *Proceedings of the 12th EPVSEC*, Amsterdam, 1994, pp. 1339–1342.

[24] J. Chandezon, et al., A new theoretical method for diffraction gratings and its numerical application, *J. Opt.* 11 (1980) 235.

[25] J.D. Hylton, Light coupling and light trapping in alkaline etched crystalline silicon wafers of solar cells, Ph.D. Thesis, University Utrecht, The Netherlands, 2006.

[26] S. Winderbaum, et al., Unveiling the differences between dynamic and static deposition of PECVD SiN for silicon solar cells, in: *Proceedings of the 20th European Solar Energy Conference*, 2005, pp. 1301–1304.

[27] A.R. Burgers, private communication.

[28] J.H. Bultman, et al., Pin-up module: a design for higher efficiency, easy module manufacturing and attractive appearance, in: *Proceedings of the 16th European Photovoltaic Solar Energy Conference*, 2000, pp. 1210–1213.

[29] J.M. Gee, et al., Progress on the emitter wrap-through silicon solar cell, in: *Proceedings of the 12th European Solar Energy Conference*, 1994, pp. 743–746.

[30] M. Jantsch, Thesis Systemtechnische Untersuchung des Nutzungsgrades Photovoltaischer Anlagen, VDI-verlag GmbH, Düsseldorf, 1996, p. 29.